

Article

https://doi.org/10.1038/s41592-025-02712-4

InterpolAI: deep learning-based optical flow interpolation and restoration of biomedical images for improved 3D tissue mapping

Received: 10 April 2024

Accepted: 18 April 2025

Published online: 28 May 2025



Saurabh Joshi^{1,2,10}, André Forjaz [©] ^{1,2,10}, Kyu Sang Han [©] ^{1,2}, Yu Shen^{1,2,3}, Vasco Queiroga [©] ^{1,2}, Florin A. Selaru⁴, Marie Gérard⁵, Daniel Xenes [©] ⁶, Jordan Matelsky⁶, Brock Wester [©] ⁶, Arrate Muñoz Barrutia [©] ⁷, Ashley L. Kiemen [©] ^{1,2,3,8,9}, Pei-Hsun Wu [©] ^{1,2} & Denis Wirtz [©] ^{1,2,3,8}

Recent advances in imaging and computation have enabled analysis of large three-dimensional (3D) biological datasets, revealing spatial composition, morphology, cellular interactions and rare events. However, the accuracy of these analyses is limited by image quality, which can be compromised by missing data, tissue damage or low resolution due to mechanical, temporal or financial constraints. Here, we introduce InterpolAI, a method for interpolation of synthetic images between pairs of authentic images in a stack of images, by leveraging frame interpolation for large image motion, an optical flow-based artificial intelligence (AI) model. InterpolAI outperforms both linear interpolation and state-of-the-art optical flow-based method XVFI, preserving microanatomical features and cell counts, and image contrast, variance and luminance. InterpolAI repairs tissue damages and reduces stitching artifacts. We validated InterpolAl across multiple imaging modalities, species, staining techniques and pixel resolutions. This work demonstrates the potential of AI in improving the resolution, throughput and quality of image datasets to enable improved 3D imaging.

New three-dimensional (3D) imaging techniques and algorithms that integrate large, multimodal datasets have improved assessment of tissue anatomy and heterogeneity using anatomical, molecular and -omic probes¹⁻⁸. Across 3D image modalities, a common challenge emerges: the lack of resolution due to mechanical and financial constraints or to damage and distortion of the tissue. Here, we introduce a methodology to repair and restore 3D biological imaging datasets using artificial intelligence (AI)-based image interpolation. We demonstrate

the utility of this method across serial sectioning-based and intact imaging datasets.

Both serial sectioning and intact imaging methods present resolution challenges. Methods that use serial sectioning allow for multiplexing across tens to hundreds of sections 2,9,10 . However, these methods face two resolution-limiting hurdles. First, imaging resolution is limited by section thickness, typically 4–10 μm for histology and ~40 nm for serial section transmission electron microscopy (ssTEM). Spatial

¹Department of Chemical and Biomolecular Engineering, Johns Hopkins University, Baltimore, MD, USA. ²The Johns Hopkins Institute for NanoBioTechnology, Johns Hopkins University, Baltimore, MD, USA. ³Department of Pathology, The Sol Goldman Pancreatic Cancer Research Center, Johns Hopkins School of Medicine, Baltimore, MD, USA. ⁴Department of Biomedical Engineering, Johns Hopkins University, Baltimore, MD, USA. ⁵Scenario, Covina, CA, USA. ⁶Research and Exploratory Development Department, Johns Hopkins Applied Physics Laboratory, Laurel, MD, USA. ⁷Bioengineering Department, Universidad Carlos III de Madrid and Instituto de Investigación Sanitaria Gregorio Marañón, Madrid, Spain. ⁸Department of Oncology, Johns Hopkins School of Medicine, Baltimore, MD, USA. ⁹Department of Functional Anatomy and Evolution, Johns Hopkins School of Medicine, Baltimore, MD, USA. ¹⁰These authors contributed equally: Saurabh Joshi, André Forjaz. ⊠e-mail: wirtz@jhu.edu

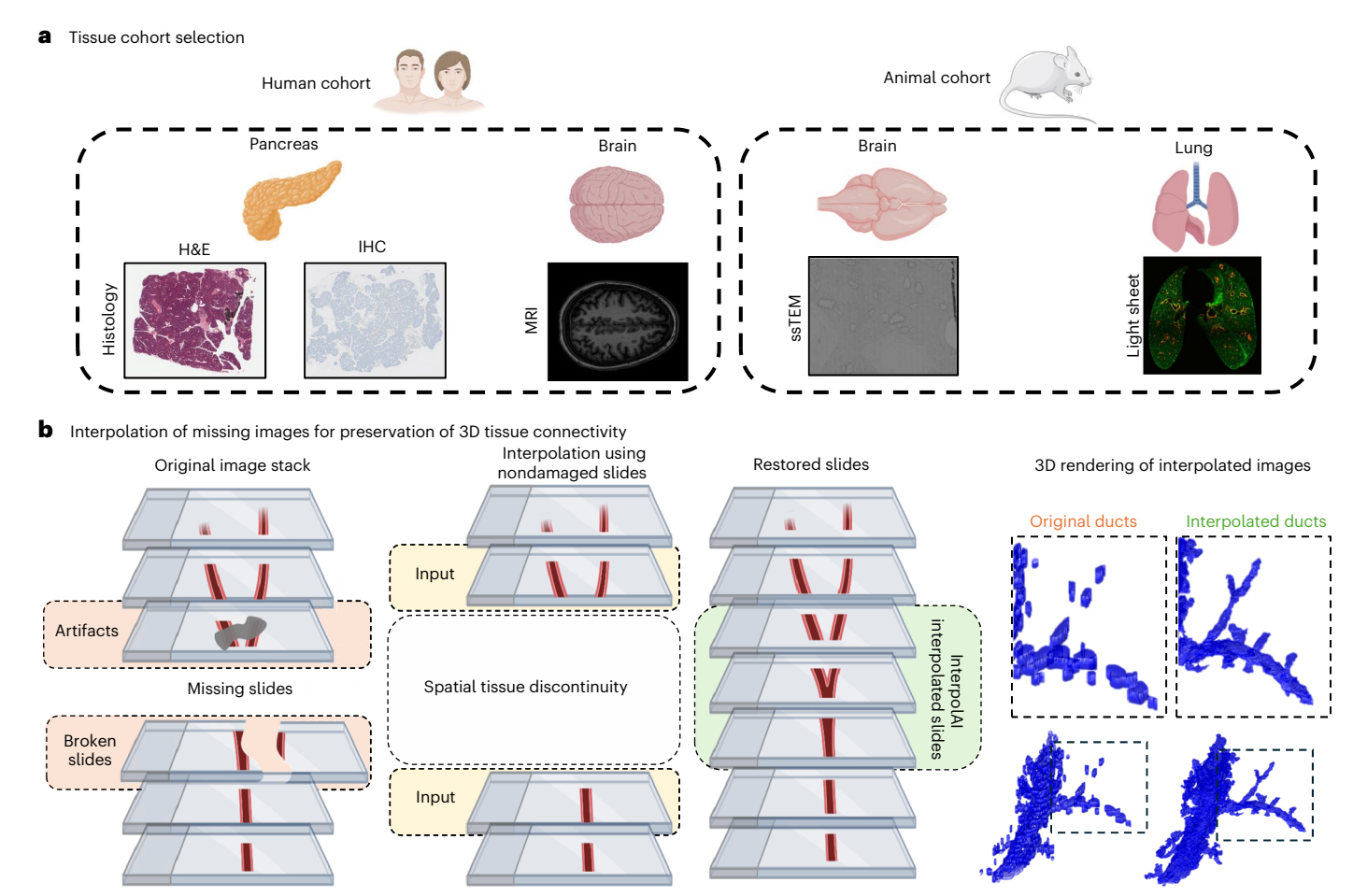


Fig. 1| **Interpolation workflow and test datasets. a**, Samples were obtained from two species, mouse and human. Four different organs were analyzed: human pancreas, human brain, mouse brain and mouse lung. Five imaging modalities were tested: H&E-stained histological slides, IHC stained histological slides, MRI, serial ssTEM slides and combined tissue clearing and light-sheet microscopy. **b**, Aligned slides are manually searched through to identify missing or damaged slides, and damaged slides are removed from the stack of slides. InterpolAl

interpolation is performed using the sections adjacent to the damaged or missing slides as inputs to recreate slides that were stained differently, missing or damaged, resulting in a uniform stack of slides. Using CODA, slides are segmented into labeled tissue masks, with each label representing a different microanatomical structure in the slide, which is then used to recreate and visualize microanatomical 3D structures in the tissue sample. Illustrations created using BioRender.com.

resolution is further limited when intermixing imaging modalities at regular intervals within the stack of tissue sections, for instance by interlacing sections stained with hematoxylin and eosin (H&E) and sections stained with antibodies via immunohistochemistry (IHC) or molecular probes via spatial transcriptomics ^{6,9–12}. Second, axial spatial resolution can be reduced by physical artifacts caused during sectioning, including tissue section splitting, folding and warping, which limit the ability to reconstruct continuous structures such as ducts and blood vessels ^{4,13,14}. In contrast, intact imaging, such as tissue clearing, magnetic resonance imaging (MRI) and computed tomography, enables 3D imaging of continuous structures ^{15–17}. However, resolution problems persist, caused by photobleaching, light absorption, motion artifacts and signal loss, which can result in loss of tissue connectivity and clarity ^{18–20}.

A promising solution lies in the application of generative models and interpolation techniques to enhance the quality of 3D reconstructions. Various generative deep learning models have been employed to synthesize tissue images, including CycleGANs (cycle-consistent generative adversarial networks) and diffusion models²¹⁻²⁸. CycleGANs are models that allow for cross-modality translation (Extended Data Fig. 1). They have been used for the transformation of H&E-stained images into their respective synthetic IHC-stained images that mark specific proteins in tissues^{23-25,29}. Diffusion models have been used to

augment MRI and computed tomography scans training datasets of deep learning models^{21,27,30}.

Despite advances in generative models, limitations persist in achieving synthetic biological images that can be used to extract accurate microanatomical information^{21–28,31–33}. Additionally, generative models are typically applied to generate different synthetic image stains of the same respective slide, but are limited in their ability to infer microanatomical structural changes across adjacent intervening slides for microanatomical 3D structure enhancement (Extended Data Fig. 1). Generation of synthetically accurate image representations of subtle or rare image texture features, cell clusters and tissue boundaries remains an unmet technical challenge^{22,26}. Here, we explore interpolation techniques, such as frame interpolation for large image motion (FILM), to restore 3D biological structures^{31–34}. We converted the video frame interpolation method FILM into a platform for spatial interpolation of synthetic biomedical images called InterpolAI. Using InterpolAI, we can propagate information contained in adjacent input slides, which restores z axis resolution of 3D microanatomical structures. Interpolation models such as InterpolAI can generate missing slides without any pevious access or knowledge of the information on those slides (Extended Data Fig. 1).

Optical flow-based models have been used for temporal interpolation and video frame upscaling, stemming from a need for more accurate and natural motion representation between frames in video sequences. The concept, which estimates the apparent motion of objects between consecutive images based on changes in brightness between frames, was first introduced in the 1980s by Horn and Schunck, who proposed a variational method to compute motion vectors in a scene³⁵. Their method assumed that certain properties of a scene, such as brightness, remained consistent between frames, allowing for the calculation of motion vectors for each pixel. These vectors describe how much and in which direction each pixel moves from one frame to the next. Early optical flow methods were computationally expensive and prone to inaccuracies and the field has since advanced with learning-based approaches. Convolutional neural networks and later models such as recurrent neural networks have improved motion prediction and image synthesis ^{36,37}.

Here, we demonstrate that interpolation of biological images using InterpolAI provides superior performance compared to the state-of-the-art optical flow model XVFI (extreme video frame interpolation)³⁸ and linear interpolation. InterpolAI-synthesized images can reconstruct microanatomical features, improve image contrast and restore cell counts in damaged or missing slides. Using InterpolAI, 3D reconstructions of semantically segmented synthetic images of complex microanatomical structures-such as ducts and blood vesselsfeature fewer artifacts than original damaged datasets, as assessed via 13 Haralick features. The versatility of InterpolAI is shown by its applications to different 3D imaging modalities (histological slides, light-sheet, ssTEM, MRI), species (human, mouse), organs (pancreas, brain, lungs) and pixel resolutions (8 nm, 2 µm, 1 mm). InterpolAl represents an important advancement by combining deep learning with motion estimation to handle large movements, making it a valuable tool for enhancing spatial resolution and recovering biological information.

Results

Multimodal tissue cohorts and interpolation workflows

We applied InterpolAI, a new interpolation workflow based on optical flow, to restore damages in stacks of two-dimensional (2D) images to recover microanatomical features lost in 3D reconstructions of tissue architecture and composition (Fig. 1)²⁷. We tested InterpolAI for a nondiseased pancreatic tissue cohort stained with H&E and IHC, a stack of ssTEM micrographs of thin sections of the mouse brain, a mouse lung tissue cleared and imaged under light-sheet microscopy, and a structural MRI dataset of the human brain. The selection of these datasets encompassed different image size and resolution, species, tissue types, imaging modalities (histology, tissue-cleared light-sheet microscopy, ssTEM, structural MRI) and magnifications. This diversity of datasets ensured that the robustness of InterpolAI was evaluated across a broad spectrum of imaging modalities.

InterpolAl uses pairs of undamaged 2D images from an image stack as inputs to improve spatial resolution or recover lost microanatomical

information (Fig. 1b). The user specifies the number of images to be interpolated based on the number of damaged or missing images in the image stack. Using the output interpolated 2D image stacks, 3D volumes can be reconstructed without missing or damaged images (Fig. 1b), which improved spatial resolution and reconstruction of tissue components in 3D (Fig. 1b).

InterpolAI interpolation for stacks of histological slides

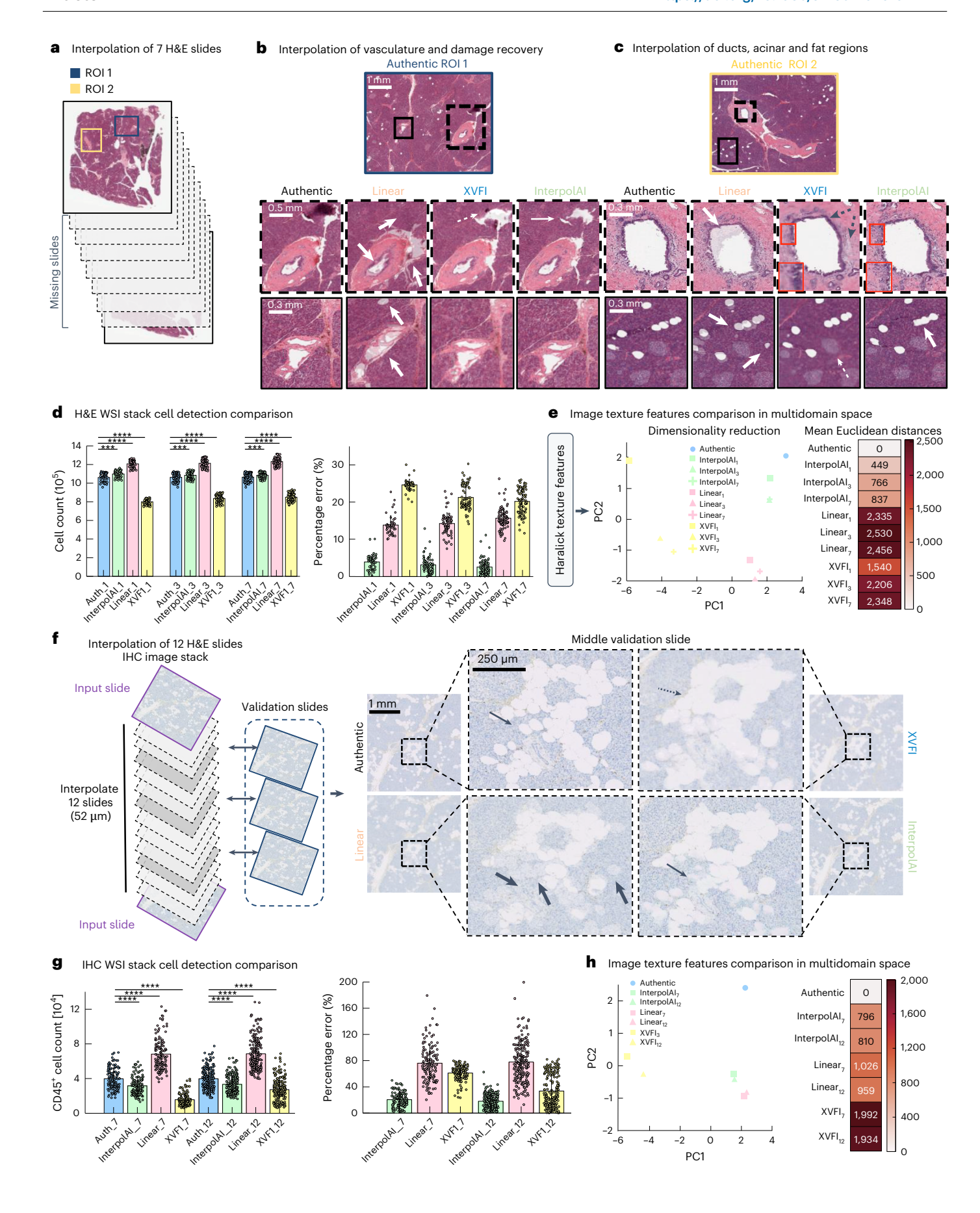
We tested the ability of InterpolAI to interpolate whole slide images (WSIs) within a stack of histological images from human pancreatic tissue samples. Histological slides are often lost or damaged due to defects created during tissue sectioning or improper storage and documentation^{13,14}. The ability of InterpolAI to interpolate slides was compared to XVFI, a state-of-the-art optical flow-based interpolation method, and linear interpolation of the same slides and then compared to the corresponding authentic slide (Fig. 2)^{32,39-41}. To qualitatively compare the interpolated slides, two regions of interest (ROI) from the 101 serially sectioned and H&E-stained human pancreas dataset were selected based on the anatomical structures present. These ROI had a total of eight tissue components, including islets of Langerhans, ductal epithelium, blood vessels, fat, acini, extracellular matrix (ECM), whitespace and PanIN (precursor) lesions. Two images were selected one every eight images (denoted skip seven) of the original stack of authentic images, and the missing seven images were interpolated (Fig. 2a). Interpolated images were compared against their respective authentic images (Fig. 2b,c).

Due to their complex branching character within the first ROI, which represent a 3D imaging challenge, we examined ducts and blood vessels (Fig. 2b). Comparison with authentic image of the duct showed that the damage was fixed by InterpolAI interpolation (top row, top arrow, Fig. 2b). In contrast, the epithelium layer of the duct showed considerable noise in the linearly interpolated image due to pixel averaging (top row, bottom arrowhead, Fig. 2b). This caused overlay artifacts that were absent in InterpolAI, which tracked pixel 'movements' using optical flow for a sharper image. Linear interpolation improperly replaced the damaged areas with acinus-like material instead of whitespace in the authentic slide (top row, top arrowhead, Fig. 2b). In contrast, InterpolAI successfully removed the damage and preserved the whitespace (top row, top arrow, Fig. 2b). Similarly to InterpolAI, XVFI removed a notable amount of damage replacing it with whitespace, however, some black damage artifacts remained (top row, top dashed arrow. Fig. 2b). Unlike InterpolAI, XVFI also incorrectly generated hued acini structures within the whitespace it interpolated (top row, right dashed arrow, Fig. 2b). Furthermore, InterpolAI preserved the central structure of the duct, whereas linear interpolation thinned and elongated the lumen (top row, middle arrowhead, Fig. 2b).

The superiority of InterpolAl over linear interpolation was further observed in blood vessels (bottom row, bottom arrowhead, Fig. 2b).

Fig. 2 | Comparison of linear, XVFI and Interpolal interpolations for pancreatic histology image stacks. a, ROI were selected from WSIs to include all microanatomical features (islets, ducts, vessels, fat, acini, ECM and PanIN). Slides were interpolated, skipping seven slides between adjacent sections. generating seven slides. b, ROI1 shows a comparison of interpolated to the authentic ROI for the middle-interpolated image for ducts and vessels. Arrowheads show linear interpolation replacing damage with acini as opposed to whitespace, creating noise around the ducts, incorrectly generating fat and unable to preserve vessel structure. Dashed arrows show XVFI removed damage, kept some black damage artifacts and incorrectly generated hued acini within the interpolated whitespace. Arrow shows InterpolAI correctly restored whitespace. c, ROI 2 shows a comparison of interpolated to the authentic ROI for the middle-interpolated image for ducts, fat and vessels. Arrowheads show linear interpolation creates duct lumen and fat shadows resembling islets as well as nonexistent fat regions. Red boxes show XVFI was unable to interpolate cellular information unlike InterpolAI. Dashed arrows show XVFI created a purple hued

band, lacking cell nuclei around the lumen of the duct. **d**, Cell counts comparison between authentic H&E and interpolated images, and percentage error in cell counts. e, PCA of 13 Haralick features for authentic, and interpolated images for various numbers of skipped images. Mean Euclidean distance of interpolated images from authentic images based on 13 Haralick features. f, IHC slides were interpolated and compared to authentic slides for validation. Middle slide is compared with the interpolated images. Arrow shows InterpolAI preserves vessel structure, unlike linear interpolation, which was also unable to preserve fat domains such as XVFI (arrowheads and dashed arrow). g, Comparison of CD45⁺ cell counts in authentic images and interpolated images when skipping 7 and 12 slides. h, PCA of 13 Haralick features for authentic and interpolated IHC images for various numbers of skipped images. Mean Euclidean distance of interpolated images from authentic images is based on 13 Haralick features. Error bars represent mean \pm s.d. * $P \le 0.05$, ** $P \le 0.01$, *** $P \le 0.001$, **** $P \le 0.0001$. Supplementary Table 2 for exact P values calculated via two-tailed Mann-Whitney *U*-test, mean and s.d.



Overlay artifacts were present throughout the entire structure of the blood vessel when using linear interpolation (bottom arrow, Fig. 2b). Unlike InterpolAI, linear interpolation could not preserve the structure of the blood vessel (Fig. 2b). Linear interpolation also incorrectly generated regions of fat that were absent in the authentic images (bottom row, top arrowhead, Fig. 2b). While XVFI accurately interpolated the structure of the blood vessel, the sharpness of the interpolated image was degraded compared to the authentic and InterpolAI images, resulting in cells in the acini that looked blurred or absent (bottom row, Fig. 2b).

In the second ROI, chosen because it was enriched in ducts, fat and islets, linear interpolation created an artificial shadow in the duct lumen (top row, top arrowhead, Fig. 2c). XVFI accurately interpolated the structure of the duct but again was unable to interpolate cellular information, specifically epithelial cells lining the duct. XVFI created a purple hued band that lacked cell nuclei around the lumen of the duct (top row, dashed arrows, Fig. 2c and inset zoom-in). In contrast, InterpolAI accurately interpolated the duct, while retaining cellular information (top row, Fig. 2c and inset zoom-in). Other key structures included fat and islets, which were typically presented as small and faint morphologies (bottom row, Fig. 2c). The authentic slide contained eight fat and five islets structures, however, linear interpolated images showed shadows of fat where real fat was located (bottom row, top arrowhead, Fig. 2c). Additionally, it generated nonexistent fat (bottom row, bottom arrowhead Fig. 2c). These fat shadows could be wrongly interpreted as islets, especially in regions where islets were present (bottom row Fig. 2c). Although InterpolAI struggled with overlapping fat, it properly interpolated distinct fat without artifacts and could clearly distinguish islets from fat.

Using CODA cell detection module, the total cell counts were computed for each of the interpolated H&E images and compared to corresponding counts in authentic images. This cell count was repeated for each scenario of skipping one, three and seven slides (Fig. 2d). Linear interpolation consistently generated images containing more cells than in the authentic images, as a result of overlay artifacts. XVFI was unable to interpolate cellular information and instead generated images that appeared blurred or out of focus, resulting in images displaying far fewer cells than the authentic images. While InterpolAI-interpolated images also generated more cells on average than in the authentic images, the percentage error in cell count for the stack of InterpolAI-interpolated images was <5% for each interpolation scenario. Linear interpolation resulted in a percentage error in cell count >10% and XVFI had a percentage error in cell count >20% for each interpolation scenario (Fig. 2d).

Thirteen Haralick features (angular second moment, contrast, correlation, sum of squares variance, inverse difference moment, sum average, sum variance, difference variance, sum entropy, difference entropy, entropy, information measure of correlation 1 and information measure of correlation 2) were measured to evaluate the quality of interpolated images 42,43. The results of each score were averaged for the different tested scenarios (authentic, InterpolAI_{skip1}, InterpolAI_{skip3}, InterpolAI_{skip7}, linear_{skip1}, linear_{skip3}, linear_{skip7}, XVFI_{skip1}, XVFI_{skip3} and XVFI_{skin7}) (Supplementary Table 1), which allowed for principal component analysis (PCA) to be carried out (Fig. 2e). This analysis demonstrated that the InterpolAI-interpolated slides represented more closely the information in the authentic slides, even when skipping seven slides, compared to linear interpolation and XVFI, which was the furthest from authentic images. The Euclidean distance of the 13 Haralick features between authentic and interpolated images was computed (Fig. 2e). Even when skipping seven slides, InterpolAl images were less than half the distance from authentic images for linearly interpolated images when skipping just one slide. When comparing independent interpolation scenarios between InterpolAI and XVFI, InterpolAI images were also less than half the distance of XVFI images to the authentic images.

Standard metrics, such as mean square error, structural similarity index measure, peak signal-to-noise ratio, Spearman correlation, Jaccard correlation, Sobel filter and channel wise pixel-to-pixel intensity correlation could not quantify the (very visible) structural errors in the microanatomical features generated by linear interpolation (Fig. 2b,c). Acini, which are the dominant structure in the healthy pancreas, could easily be interpolated, resulting in similar metric values for linear and InterpolAI, since these metrics are less sensitive to small-pixel deviations compared to large-pixel deviations. We attempted masking acini to focus on microanatomical structures, but registration differences between images only highlighted alignment issues rather than interpolation quality.

Validation with expert pathologists at the Johns Hopkins School of Medicine (GI division, Department of Pathology) was attempted to determine the authenticity of interpolated images. Initially, pathologists were unable to distinguish microanatomical differences between authentic and InterpolAI-generated images. Over time, pathologists distinguished interpolated from authentic images by their reduced damage artifacts.

In sum, InterpolAI can accurately interpolate damaged or missing H&E-stained histological images, which restores lost information in stacks of 2D images and, consequently, improves connectivity of 3D continuous microanatomical structures (additional details below). Unlike linear interpolation, InterpolAI does not generate nonexistent microanatomical structures, such as ducts or fat in pancreatic tissues, and preserves cellular information better than XVFI.

InterpolAI for IHC image stacks

To further demonstrate the ability of InterpolAl to interpolate histological WSIs, a second human pancreas sample was stained using IHC for the leukocyte marker CD45. We note the substantial distance between input slides, $52~\mu m$, equivalent to omitting $12~successive~4~\mu m$ -thick sections (Fig. 2f). The target images, for which authentic validation slides were available for comparison, are shaded in dark gray, while the missing slides between the input and target slides are shaded in light gray (Fig. 2f).

We compared the middle-interpolated slide to the middle authentic validation slide using both linear and InterpolAI models (Fig. 2f). In fat dense regions, linear interpolation artifacts were evident, while InterpolAI lacked such artifacts (arrow, Fig. 2f). Additionally, whereas distinct cells were readily identified in the authentic image, the linearly interpolated image showed faintly stained cells covered with white hues resembling fat (right arrowhead, Fig. 2f). Similarly, XVFI generated slides showed faded and blurred cells and did not accurately preserve the structure of fat regions, which lacked edges and resembled whitespace (dashed arrow, Fig. 2f). In contrast, InterpolAI could interpolate distinct cells around the fat and preserved most of the ductal and ECM structures (arrow, Fig. 2f), unlike the linear interpolation (left arrowhead, Fig. 2f).

Using CODA, the total cell count of CD45 positive (CD45⁺) cells was determined for linear, XVFI and InterpolAI-interpolated images and compared to the cell counts in the authentic images, while skipping and interpolating 7 and 12 slides. Linear interpolation resulted in higher CD45⁺ cell counts than those in authentic slides. Conversely, XVFI interpolation resulted in cell counts far lower than those in the authentic slides. InterpolAI-interpolated slides resulted in lower cell counts than in the authentic slides, but most closely matched the cell count trend in authentic slides (Fig. 2g). Linearly interpolated slides had the highest percentage error in CD45⁺ cell count, reaching more than 100% for certain slides, followed by XVFI and InterpolAI-interpolated slides, with a mean error of 22% in cell count (Fig. 2g).

Thirteen Haralick texture features were evaluated when interpolating 7 and 12 slides. The results of each score were averaged for the different scenarios assessed (authentic, InterpolAI $_{skip7}$, InterpolAI $_{skip12}$, linear $_{skip7}$, linear $_{skip7}$, and XVFI $_{skip12}$) (Supplementary Table 1).

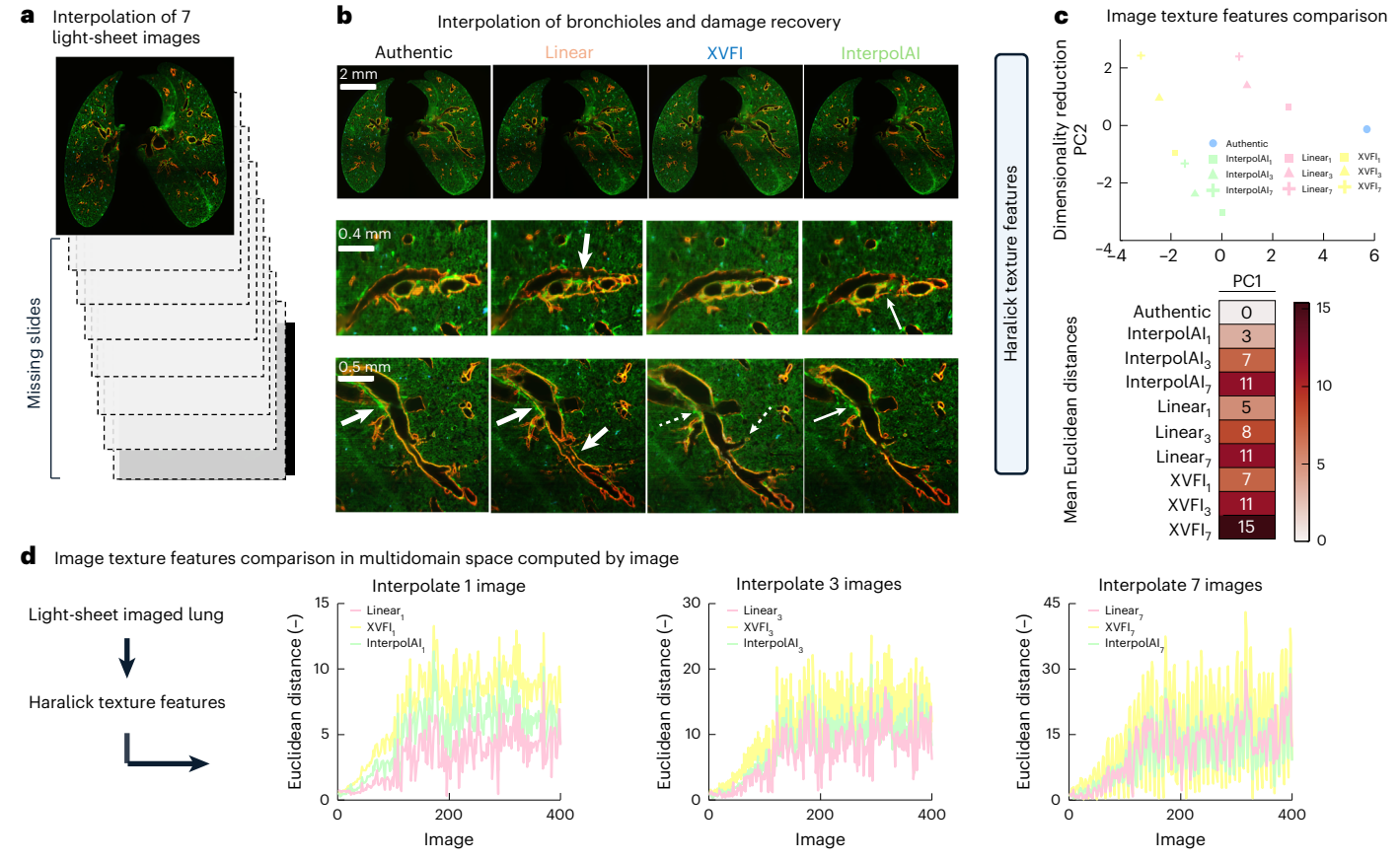


Fig. 3 | **InterpolAl interpolation for stacks of MRI and light-sheet microscopy images. a**, Tissue-cleared light-sheet images were interpolated skipping seven slides between adjacent sections, thereby generating seven slides. **b**, Qualitative comparison of linear, XVFI and InterpolAl interpolations to the authentic image for the middle-interpolated light-sheet image (image 4). Arrowhead shows linear interpolation creates double boundary lines around bronchioles. In the second row, the arrowhead shows photobleaching in authentic reduced by linear interpolation and completely removed by InterpolAl (arrow). Dashed arrow

shows XVFI reduced photobleaching but did not remove it. Second dashed arrow shows XVFI elongated the right edge of a bronchiole. ${\bf c}$, PCA of 13 Haralick features for authentic, linear, XVFI and InterpolAl-interpolated light-sheet images for various numbers of skipped light-sheet images. Mean Euclidean distance of interpolated images from authentic images based on 13 Haralick features. ${\bf d}$, Euclidean distance by slide of interpolated images from authentic images based on 13 Haralick features for various numbers of skipped light-sheet images.

PCA analysis showed that InterpolAI-interpolated slides more closely represented authentic slide information along principal component 1 and linear along component 2, while XVFI interpolated slides were the furthest away (Fig. 2h). The measurement of the Euclidean distance between authentic and interpolated images demonstrated that InterpolAI $_{\rm skipI2}$ more closely represented the authentic slides compared to both linear $_{\rm skip7}$ and XVFI $_{\rm skip7}$ (Fig. 2h).

In sum, by interpolating IHC-CD45 stained images and determining the difference in cell count between authentic and interpolated images, we show the ability of InterpolAI to interpolate not only multicellular structures in stacks of histological images, such as ducts and blood vessels, but also smaller features, such as individual cells.

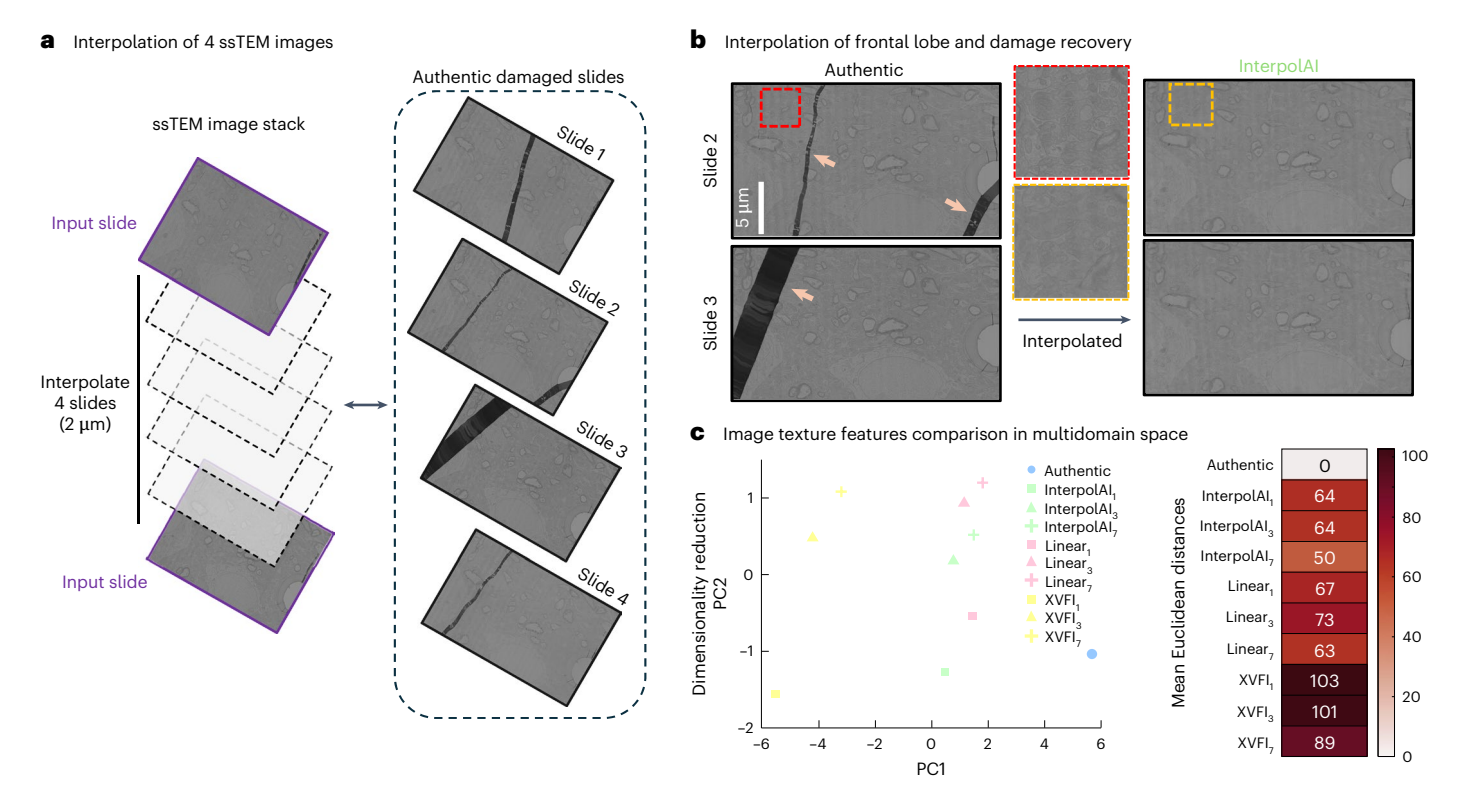
InterpolAI for stacks of light-sheet microscopy images

Next, we applied InterpolAl to interpolate images within a stack of light-sheet micrographs obtained from a cleared mouse lung. Light-sheet microscopy presents challenges, including photobleaching and light absorption, which may result in uneven illumination of the sample, and tissue movement during imaging, which can introduce further distortions. Pairs of images were selected skipping seven images from the authentic stack (Fig. 3a), and interpolated images were compared to their authentic counterparts.

Linear interpolation of light-sheet micrographs created artificial double boundary lines around the bronchioles, which is biologically

inaccurate (middle row, top arrowhead, Fig. 3b) (bottom row, right arrowhead, Fig. 3b). Similarly, XVFI created two additional bronchioles that do not exist in the authentic image inaccurate (middle row, dashed arrow, Fig. 3b) and elongated the right edge of a bronchiole (bottom row, right dashed arrow, Fig. 3b). In contrast, InterpolAI correctly interpolated images of bronchioles to accurately depict the structure observed in the authentic image (middle row, arrow, Fig. 3b). The second row of zoom-ins shows that the authentic image suffers from artifacts of light absorption and photobleaching at the top left of the bronchiole, which cause bleeding of the green and red channels into the bronchiole (bottom row, left arrowhead, Fig. 3b). Both linear interpolation and XVFI reduced these artifacts, but could not remove them entirely (bottom row, left arrowhead and left dashed arrow, Fig. 3b), whereas InterpolAI removed the bleed of the red and green channels (bottom row, left arrow, Fig. 3b).

Thirteen Haralick texture features were measured to compare authentic and interpolated images, when interpolating one, three and seven slides. The results for each score were averaged for the different comparisons (authentic, InterpolAl $_{\rm skip1}$, InterpolAl $_{\rm skip3}$, InterpolAl $_{\rm skip3}$, InterpolAl $_{\rm skip7}$, linear $_{\rm skip3}$, linear $_{\rm skip3}$, $\rm VVFl_{\rm skip1}$, $\rm VVFl_{\rm skip3}$ and $\rm VVFl_{\rm skip7}$) (Supplementary Table 1), and shown in a PCA plane (Fig. 3c). PCA analysis showed that linearly interpolated images were more closely representative of the authentic images compared to InterpolAl and XVFI interpolated images (Fig. 3c). Nevertheless, when considering the mean



 $\label{linear} \textbf{Fig. 4} | \textbf{InterpolAl interpolation for a stack of ssTEM images. a}, \textbf{ssTEM slides} \\ were interpolated while skipping four slides between adjacent sections, thereby generating four slides. \textbf{b}, InterpolAl interpolation of mouse brain ssTEM slides to remove damage from slides (arrowheads) and reduce stitching artifacts$

 $(red \, box). \, \boldsymbol{c}, PCA \, of \, 13 \, Haralick \, features \, for authentic, linear, XVFI \, and \, InterpolAl-interpolated \, ssTEM \, images \, for various \, skipped \, images. \, Mean Euclidean \, distance \, of interpolated \, images \, from \, authentic \, images \, based \, on \, 13 \, Haralick \, features.$

Euclidean distance, InterpolAI outperformed linear interpolation for each individual skip scenario and outperformed XVFI when skipping one and three slides (Fig. 3c). The Euclidean distance by slide increased when interpolating using XVFI or interpolating linearly through the stack as opposed to InterpolAI, which remained consistent through the stack (Fig. 3d).

In sum, InterpolAI can interpolate stacks of light-sheet images to reduce photobleaching and light absorption artifacts present in the authentic images, better than XVFI and linear interpolation. Elimination of such artifacts allows for more accurate 3D reconstructions of tissue samples.

InterpolAI interpolation and restoration of ssTEM images

A stack of serial ssTEM micrographs of the mouse brain was used to show our ability to interpolate not only histological sections (Fig. 4a). The authentic tiles shown Fig. 4a represent a $2,000 \times 3,500$ -pixel tile of the authentic WSI. Thick irregular black lines were observed across most of the slides in the authentic stack of images, which correspond to damage caused by unavoidable tissue tear during processing of thin sections (left column, arrows, Fig. 4b). For a randomly selected subset of 100 consecutive slides from a stack of the >13,000 ssTEM slides, we found that >70% were damaged, many of them containing more than one damaged region. Additionally, fainter gray lines were observed, going horizontally across the authentic images, which are artifacts of image stitching (top row, bound by red box Fig. 4b).

Interpolation between two undamaged ssTEM slides using Interpolal removed the damage to the slides while preserving their microanatomical structures, but also substantially reduce stitching artifacts (right column, Fig. 4b).

Thirteen Haralick features were measured for the authentic and interpolated images when interpolating one, three and seven slides. The results of each score were averaged for the different tested

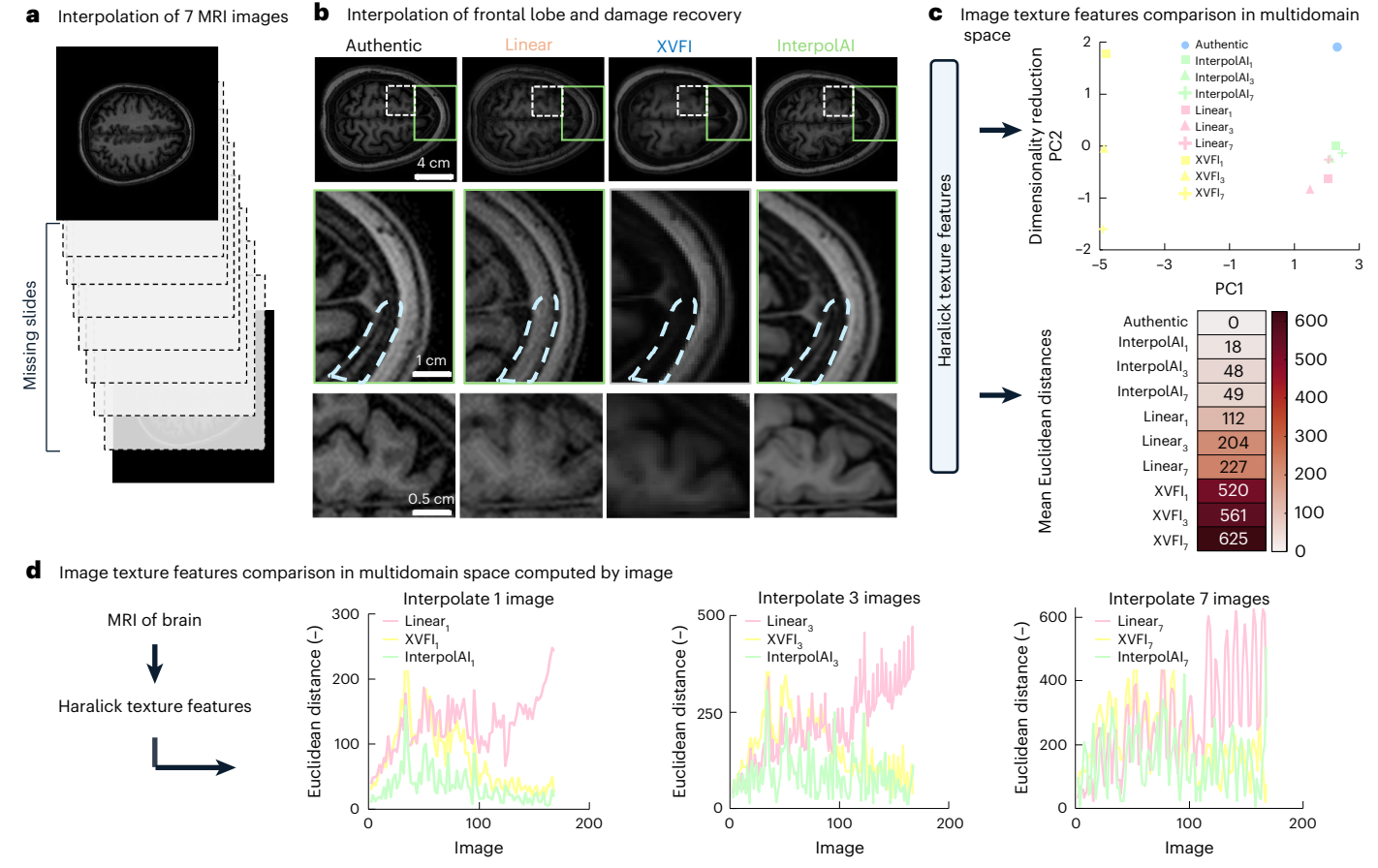
scenarios (authentic, InterpolAl $_{skip1}$, InterpolAl $_{skip3}$, InterpolAl $_{skip7}$, linear $_{skip3}$, linear $_{skip3}$, linear $_{skip3}$, linear $_{skip3}$, XVFI $_{skip3}$ and XVFI $_{skip7}$) (Supplementary Table 1). PCA showed that InterpolAl-interpolated slides more closely represented authentic slide information along principal component 2, while linear along component 1 and XVFI being the furthest away (Fig. 4c). The short Euclidean distance between authentic and interpolated images suggests that InterpolAl $_{skip1}$ more closely represents the authentic than linear $_{skip1}$ and XVFI $_{skip1}$ and similarly for the instance of skipping three and seven slides (Fig. 4c).

In sum, we demonstrated the ability of InterpolAl to eliminate damage in ssTEM slides, allowing for more accurate 3D reconstructions of neural structures by decreasing the loss in connectivity that arises due to the damage in individual 2D sections.

Interpolal interpolation for stacks of MRI images

To assess the ability of InterpolAI to interpolate low-resolution biomedical images, we interpolated images within stacks of MRI images $(1\times1\times1\,\text{mm})$. MRI faces inherent limitations, such as susceptibility to motion artifacts due to prolonged scan times leading to patient discomfort and potential for signal loss due to magnetic field inhomogeneities that can affect the quality of acquired images. Pairs of images were selected one every eight images (skip seven) of the original stack of authentic images, and the missing seven images were interpolated (Fig. 3a). Interpolated images were validated against their respective authentic images (Fig. 3b).

Linear interpolation of MRI images caused band artifacts around the boundary of the soft tissue, unlike XVFI and InterpolAI (middle row, Fig. 5b). However, as a result of thicker slices obtained during MRI (1 mm), InterpolAI could not always accurately interpolate large structural changes in soft tissue structures that occur when skipping seven images (8 mm) (bottom row, Fig. 5b). Nevertheless, linear interpolation created a structure that resembled a gray smudge with notable overlay



 $\label{limiter} \textbf{Fig. 5} | \textbf{InterpolAl interpolation for a stack of MRI images. a}, MRI images were interpolated while skipping seven slides between adjacent sections, thereby generating seven slides.$ **b**, Qualitative comparison of linear, XVFI and InterpolAl interpolation to the authentic image for the middle-interpolated MRI (image 4). The circled region shows linear interpolation creates band artifacts, unlike XVFI and InterpolAl.**c**, PCA of 13 Haralick features for authentic, linear, XVFI and

Interpolal-interpolated MRI images for various numbers of skipped images. Mean Euclidean distance of interpolated images from authentic images based on 13 Haralick features. ${\bf d}$, Euclidean distance by slide of interpolated images from authentic images based on 13 Haralick features for various numbers of skipped MRI images.

artifacts, while XVFI created a faint and inaccurate structure (bottom row, Fig. 5b), unlike InterpolAI.

Thirteen Haralick texture features were measured to compare authentic and interpolated MRI images, when interpolating one, three and seven slides. The results for each score were averaged for the different comparisons (Supplementary Table 1), and shown in a PCA plane (Fig. 5c). InterpolAI-interpolated slides represented more closely the information in the authentic slides, even when skipping seven slides, compared to linear interpolation and XVFI, which was the furthest. The averaged values were also used to compute the Euclidean distance between authentic and interpolated images (Fig. 5c). Skipping seven slides, InterpolAI-interpolated slides were less than half the Euclidean distance between the authentic slides and the linearly or XVFI interpolated slides when skipping only one slide. The Euclidean distance by slide further emphasizes the superiority of InterpolAI over linear interpolation as the Euclidean distance increased when progressing through the stack of slides and interpolating linearly as opposed to InterpolAI (Fig. 5d).

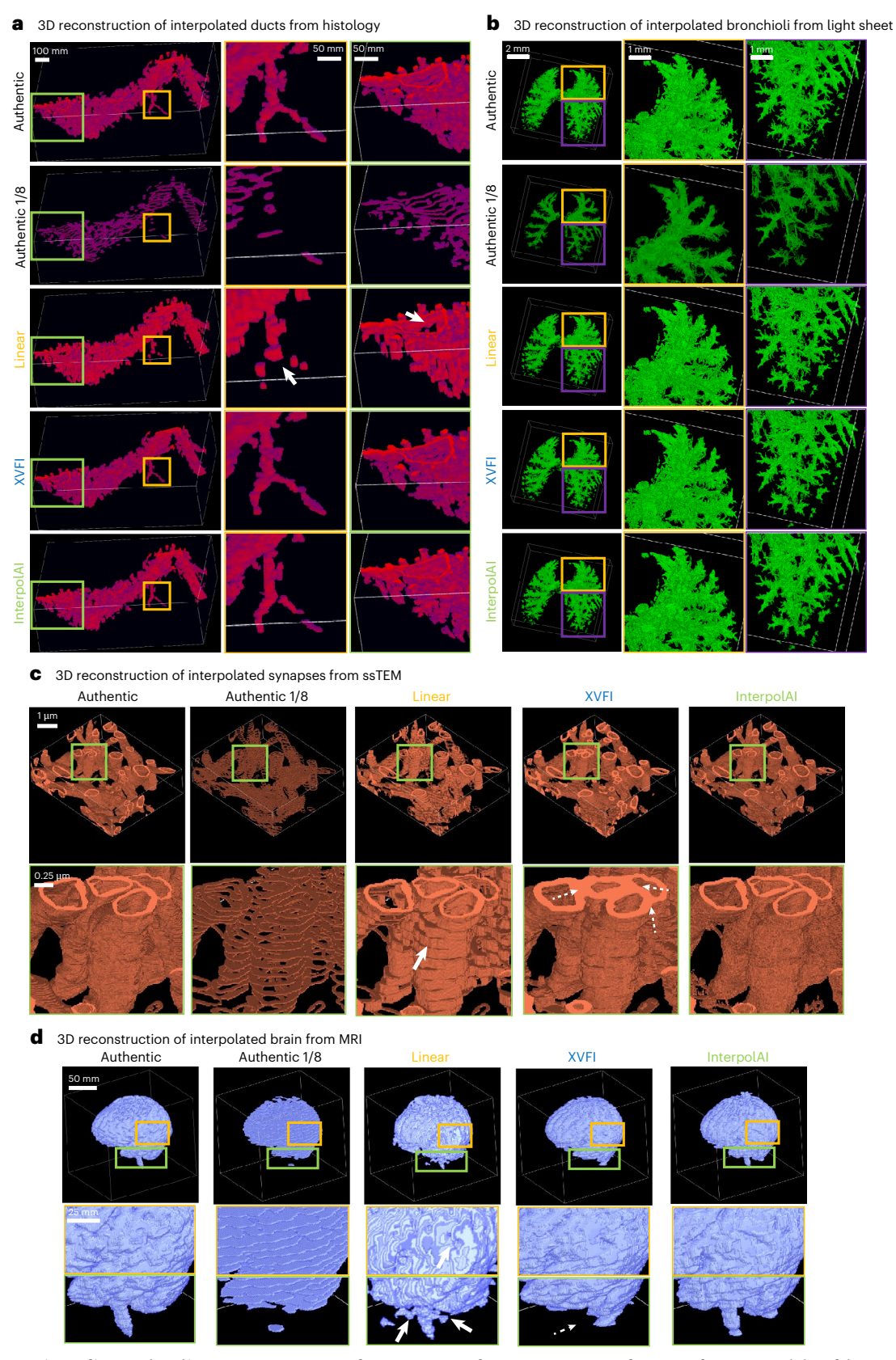
We demonstrated the ability of InterpolAI to interpolate low-resolution MRI images more accurately than linear and XVFI interpolations. InterpolAI reduces motion artifacts in MRI images, whereas linear interpolation exaggerates these artifacts, which result in band artifacts. Elimination of such artifacts allows for improved 3D reconstructions of whole organ structures. However, shorter interpolation distances might be required to account for large structural changes that occur as a result of the low z resolution of MRI.

$3D\,reconstruction\,of\,InterpolAI\text{-}interpolated\,images$

To demonstrate the application of InterpolAI to restore 3D images of microanatomical structures obtained from interpolated 2D images, InterpolAI interpolation was applied across different image modalities, including stacks of histological (H&E and IHC), light-sheet, ssTEM and MRI images. Sematic segmentation and subsequent concatenation of the 2D segmented images into a volume allowed visualization of microanatomical features in 3D.

Using CODA, we reconstructed in 3D the epithelial duct from the pancreatic H&E dataset (Fig. 6a). The 3D reconstruction of the authentic volume skipping seven images displays the loss in ductal connectivity resulting from the missing slides. Linear interpolation of the H&E samples created a low-resolution 3D structure of the duct that was artificially blocky (that is not smooth), and did not preserve the branching morphology of the duct (yellow zoom-in, arrowhead, Fig. 6a). Linear interpolation also generated ductal structures that in parts missed their ductal wall (green zoom-in, arrowhead, Fig. 6a). In contrast, InterpolAI and XVFI restored the microanatomical connectivity in the 3D reconstruction of the main and smaller branches of the duct, while also creating a smoother volume without noise propagation (Supplementary Video 1). Although structurally accurate, XVFI compromised the identification of cells in H&E images as demonstrated in Fig. 2d.

Tissue-cleared light-sheet images were separated by channel and used to reconstruct in 3D the bronchioles of a mouse lung (Fig. 6b). The



 $\label{eq:Fig.6} \textbf{Fig. 6} | \textbf{3D reconstructions of interpolated images. a}, \textbf{C} omparison of 3D reconstructions of human pancreatic duct from a stack of H&E sections, when skipping seven slides between authentic images and when interpolating the missing slides using linear, XVFI and InterpolAl interpolations.$ **b**, Comparison of 3D reconstructions of bronchioles from light-sheet images of the mouse lung when skipping seven images between authentic images and when interpolating the missing slides using linear, XVFI and InterpolAl interpolations.**c**, Comparison

of 3D reconstructions of synapses from ssTEM slides of the mouse brain when skipping seven images between authentic images and when interpolating the missing slides using linear, XVFI and Interpolal interpolations. ${\bf d}$, Comparison of 3D reconstructions of brain MRI images when skipping seven images between authentic images and when interpolating the missing slides using linear, XVFI and Interpolal interpolations.

comparison of the authentic volume to a downsampled reconstruction of the authentic volume (skipping seven images between adjacent z planes) showed a loss in connectivity of the bronchioles in 3D as a result of the missing image scans. The use of all three interpolation methods to recover missing z planes resulted in improved connectivity of the bronchioles in 3D (Fig. 6b). The results in 3D matched those observed in 2D (Fig. 3), where all three interpolation methods were comparable in performance as demonstrated through 13 Haralick texture features.

Next, segmented ssTEM images were interpolated using linear, XVFI and InterpolAI interpolation to reconstruct in 3D the synapses of the mouse brain. A qualitative assessment between the authentic volume and downsampled recreation of the authentic volume (skipping seven images between adjacent z planes) shows the loss in synapse connectivity (Fig. 6c). Linear interpolation to recover the missing z planes results in the creation of a low-resolution volume with blocky structures (green zoom-in, arrowhead, Fig. 6c). Similarly, XVFI created a low-resolution volume, although less blocky than linear interpolation. Additionally, XVFI generated connected synapses as opposed to distinct tubules seen in the authentic volume (green zoom-in, dashed arrows, Fig. 6c). Conversely, InterpolAI interpolation resulted in a higher resolution 3D volume, which resembled that of the authentic volume, and allowed for synapse connectivity to be restored (Supplementary Video 2).

Finally, CODA was used to reconstruct a whole human brain in 3D using the stack of MRI images. A comparison of the reconstructed authentic volume to the authentic volume skipping seven images showed how connectivity was lost as a result of the missing images. The reconstructed authentic volume skipping seven images also lacked the topographical structure of the brain seen in the authentic volume. replacing it with single planes of information (Fig. 6d). Using linear interpolation to recover the missing or damaged scans resulted in increased edges, which resembled objects extruding abnormally out of the brain. This is especially evident around the base of the brain where the brain stem protrudes and at the top of the brain toward the skull cap (green zoom-in, arrowhead, Fig. 6d). Linear interpolation also generated a biologically inaccurate topography of the brain (yellow zoom-in, arrowhead, Fig. 6d). XVFI generated a volume accurate in topography but failed to interpolate branching structures in the brain, specifically the brain stem (green zoom-in, dashed arrow, Fig. 6d). When interpolating images using InterpolAI, the 3D reconstructed volume resembled more closely that of the authentic one, with accurate indentations and topography around the surface of the brain and even accurate reconstruction of the branching brain stem structure.

In sum, missing or damaged slides and images in biomedical image stacks cause substantial loss in 3D spatial information, which hinders the accurate 3D reconstruction of microanatomical structures and whole organs from these image stacks. We demonstrate that linear interpolation is not sufficiently robust to recover the information lost in complex biomedical images, resulting in inaccurate 3D reconstructions. While XVFI interpolation preserves the structural connectivity of most microanatomical structures, it is limited in its ability to generate distinct and disjointed structures as seen with the ssTEM dataset. Additionally, as observed with the H&E histology dataset XVFI cannot preserve the single-cell resolution found in H&E images (Fig. 2). In contrast, the optical flow-based model InterpolAI recovers more information to allow for 3D reconstructions that qualitatively and quantitively resemble their authentic counterparts.

Discussion

The 3D imaging of biomedical samples has become a requirement as 2D assessments are not sufficient in capturing the content and morphology of multicellular structures, rare events and spatial relationships among different cell types¹. A multitude of platforms have been developed to leverage 2D biomedical stacks of histological, ssTEM and tissue-cleared light-sheet images to reconstruct volumes

of microanatomical structures and whole organs. Such platforms are highly dependent on the quality of individual 2D images within the image stacks for accurate volumetric reconstructions. Additionally, limitations in the *z* resolution of these 3D platforms often arise due to missing slides, tissue damage and the high cost associated with 3D imaging.

Here, we address these challenges by introducing InterpolAI and its ability to extract and track features in biomedical images using optical flow for image interpolation. By interpolating between undamaged slides to recover missing or damaged slides, we bridge gaps in z resolution. This workflow restores the connectivity of continuous microanatomical structures, such as ducts and blood vessels, in the 3D reconstructions and mitigates issues arising from damaged or missing slides. This method improves 2D biomedical image stacks for 3D reconstructions, subsequently improving quantitative assessments of cellular composition, tissue topography and degree of branching of continuous structures.

We conducted a thorough comparative assessment of the Interpolal Platform to linear and XVFI interpolation methods using 13 Haralick texture features. Linear interpolation, which averages pixel intensities that create hued colors and structures, cannot create realistic biomedical images. As the number of images skipped increases, linearly interpolated images further degrade in authenticity, especially for the images furthest from the input images (middle-interpolated image). For large number of skipped images (for example, skip seven), the middle-interpolated image presents strong hues as pixel intensities deviate largely between input images. XVFI interpolation, on the other hand, could more accurately generate synthetic biomedical images than linear interpolation, however, XVFI was unable to achieve cellular resolution and was often limited in its ability to restore damage in images. Conversely, InterpolAI can interpolate biomedical images that resemble their authentic counterparts.

For light-sheet microscopy, InterpolAI accurately interpolates images in the z direction reducing required z steps during image acquisition. This decreases imaging times of an entire sample, as imaging patterns are often imaged tile by tile laterally before moving to the next z level. Collection time increases exponentially with the lateral size of the sample, from minutes for a 10^4 μ m 3 sample at a spatial resolution of 500 nm to a week for a 10^8 μ m 3 sample at the same resolution 16 . InterpolAI interpolation helps address this limitation.

InterpolAI has a few limitations, which must be considered for optimal interpolation results. First, InterpolAI requires well-aligned images for optimal interpolation. Using misaligned images leads to model hallucinations, which appear as unrealistic biological structures (Supplementary Fig. 1). InterpolAI handle vertical and horizontal misalignments well, up to a misalignment distance of 200 µm. However, Interpolal cannot successfully interpolate images when they are bi-directionally or diagonally misaligned beyond a distance of 200 µm or rotated beyond 2°. Second, InterpolAI performs best when using nondamaged images as input pairs, which can result in the damage being propagated across the interpolated images. This is shown in the damage assessment carried out in Supplementary Fig. 2b,f where positive data (+yaxis) points show damage being propagated in interpolated images as a result of damaged inputs and negative data (-y axis) points show damage being restored. Aside from obvious damage in input images such as tissue folds and tears, stain inconsistencies are an important consideration as sudden changes in pixel intensity and illumination between input images can cause model hallucinations. Last, InterpolAI generates images based on the two input images provided and therefore cannot predict rare events, which did not occur on either of the input images. This is also noticeable from the results obtained using the MRI dataset with thicker slices (1 mm) compared to thinly sliced ssTEM, tissue-cleared light-sheet microscopy and histology images (8 nm, 2 µm). InterpolAl could not accurately predict large structural changes in MRI images when skipping seven slides (8 mm).

In conclusion, our work goes beyond existing methods of image translation, such as CycleGANs and diffusion models that translate the same respective biomedical images from one image domain to another. Whereas image translation would require physical access to the slides of interest to be translated, our workflow interpolates missing, inaccessible or damaged images, eliminates stitching artifacts and works across diverse multimodal biomedical images (Extended Data Fig. 1). Future work could extend InterpolAl's application to other spatial omics platforms, enhancing the integration of transcriptomic, proteomic and metabolomic data with 3D tissue structures. This would allow for a more precise multimodal analysis and high-resolution tissue atlases.

Online content

Any methods, additional references, Nature Portfolio reporting summaries, source data, extended data, supplementary information, acknowledgements, peer review information; details of author contributions and competing interests; and statements of data and code availability are available at https://doi.org/10.1038/s41592-025-02712-4.

References

- Forjaz, A. et al. Three-dimensional assessments are necessary to determine the true spatial tissue composition of diseased tissues. Preprint bioRxiv https://doi.org/10.1101/2023.12.04.569986 (2023).
- Kiemen, A. L. et al. CODA: quantitative 3D reconstruction of large tissues at cellular resolution. *Nat. Methods* 19, 1490–1499 (2022).
- Cline, H. E., Dumoulin, C. L., Hart, H. R., Lorensen, W. E. & Ludke, S. 3D reconstruction of the brain from magnetic resonance images using a connectivity algorithm. *Magn. Reson. Imaging* 5, 345–352 (1987).
- The MICrONS Consortium. Functional connectomics spanning multiple areas of mouse visual cortex. *Nature* 640, 435–447 (2025).
- Yin, W. et al. A petascale automated imaging pipeline for mapping neuronal circuits with high-throughput transmission electron microscopy. Nat. Commun. 11, 4949 (2020).
- Bell, Alexander T. F. et al. PanIN and CAF transitions in pancreatic carcinogenesis revealed with spatial data integration. *Cell Syst.* https://doi.org/10.1016/j.cels.2024.07.001 (2024).
- Maitin-Shepard, J. et al. google/neuroglancer. Zenodo https://doi.org/ 10.5281/zenodo.5573294 (2021).
- Kiemen, A. L. et al. Tissue clearing and 3D reconstruction of digitized, serially sectioned slides provide novel insights into pancreatic cancer. Med 4, 75–91 (2023).
- Lin, J. R. et al. Multiplexed 3D atlas of state transitions and immune interaction in colorectal cancer. *Cell* 186, 363–381.e19 (2023).
- Crawford, A. J. et al. Combined assembloid modeling and 3D whole-organ mapping captures the microanatomy and function of the human fallopian tube. Sci. Adv. 10, eadp6285 (2024).
- Sans, M. et al. Spatial transcriptomics of intraductal papillary mucinous neoplasms of the pancreas identifies NKX6-2 as a driver of gastric differentiation and indolent biological potential. *Cancer Discov.* 13, 1844–1861 (2023).
- Liu, Y. et al. High-spatial-resolution multi-omics sequencing via deterministic barcoding in tissue. Cell 183, 1665–1681.e18 (2020).
- McInnes, E. Artefacts in histopathology. Comp. Clin. Pathol. 13, 100–108 (2005).
- Taqi, S. A., Sami, S. A., Sami, L. B. & Zaki, S. A. A review of artifacts in histopathology. J. Oral. Maxillofac. Pathol. 22, 279 (2018).
- Glaser, A. K. et al. A hybrid open-top light-sheet microscope for versatile multi-scale imaging of cleared tissues. *Nat. Methods* 19, 613 (2022).
- Daetwyler, S. & Fiolka, R. P. Light-sheets and smart microscopy, an exciting future is dawning. Commun. Biol. 6, 502 (2023).

- Kubota, S. I. et al. Whole-organ analysis of TGF-β-mediated remodelling of the tumour microenvironment by tissue clearing. Commun. Biol. 4, 294 (2021).
- Nárai, Á. et al. Movement-related artefacts (MR-ART) dataset of matched motion-corrupted and clean structural MRI brain scans. Sci. Data 9, 630 (2022).
- Gilmore, A. D., Buser, N. J. & Hanson, J. L. Variations in structural MRI quality significantly impact commonly used measures of brain anatomy. *Brain Inform.* 8, 7 (2021).
- Krupa, K. & Bekiesińska-Figatowska, M. Artifacts in magnetic resonance imaging. *Pol. J. Radio.* 80, 93 (2015).
- Khader, F. et al. Denoising diffusion probabilistic models for 3D medical image generation. Sci. Rep. 13, 7303 (2023).
- Kazerouni, A. et al. Diffusion models in medical imaging: a comprehensive survey. Med. Image Anal. 88, 102846 (2023).
- Bai, B. et al. Deep learning-enabled virtual histological staining of biological samples. *Light Sci. Appl.* https://doi.org/10.1038/ s41377-023-01104-7 (2023).
- Koivukoski, S., Khan, U., Ruusuvuori, P. & Latonen, L. Unstained tissue imaging and virtual hematoxylin and eosin staining of histologic whole slide images. *Lab. Invest.* 103, 100070 (2023).
- Kang, L., Li, X., Zhang, Y. & Wong, T. T. W. Deep learning enables ultraviolet photoacoustic microscopy based histological imaging with near real-time virtual staining. *Photoacoustics* 25, 100308 (2022).
- Deshpande, S., Dawood, M., Minhas, F. & Rajpoot, N. SynCLay: interactive synthesis of histology images from bespoke cellular layouts. *Med. Image Anal.* 91, 102995 (2024).
- Li, Y. et al. Zero-shot medical image translation via frequency-guided diffusion models. *IEEE Trans. Med. Imaging* 43, 980–993 (2023).
- 28. Cross-Zamirski, J. O. et al. Class-guided image-to-image diffusion: cell painting from Brightfield images with class labels. In 2023 IEEE/CVF International Conference on Computer Vision Workshops (ICCVW) 3802–3811 (IEEE, 2023).
- 29. Xu, Z., Huang, X., Moro, C. F., Bozóky, B. & Zhang, Q. GAN-based virtual re-staining: a promising solution for whole slide image analysis (2019).
- Ho, J., Jain, A. & Abbeel, P. Denoising diffusion probabilistic models. Adv. Neural Inf. Process Syst. 33, 6840–6851 (2020).
- Gaffling, S., Jäger, F., Daum, V., Tauchi, M. & Lütjen-Drecoll, E. Interpolation of histological slices by means of non-rigid registration. In *Bildverarbeitung für die Medizin 2009* https://www5.informatik.uni-erlangen.de/Forschung/ Publikationen/2009/Gaffling09-IoH.pdf (2009).
- Leng, J., Xu, G. & Zhang, Y. Medical image interpolation based on multi-resolution registration. *Comput. Math. Appl.* 66, 1–18 (2013).
- 33. Akhtar, P. & Azhar, F. A single image interpolation scheme for enhanced super resolution in bio-medical imaging. In *Proc. 2010 4th International Conference on Bioinformatics and Biomedical Engineering, iCBBE 2010* 1–5 (IEEE, 2010).
- 34. Reda, F. A. et al. FILM: frame interpolation for large motion. Preprint at https://arxiv.org/abs/2202.04901 (2022).
- 35. Horn, B. K. P. & Schunck, B. G. Determining optical flow. *Artif. Intell.* **17**, 185–203 (1981).
- Hu, P., Wang, G. & Tan, Y.-P. Recurrent spatial pyramid CNN for optical flow estimation. *IEEE Trans. Multimed.* 20, 2814–2823 (2018).
- 37. Hui, T.-W., Tang, X. & Loy, C. C. A lightweight optical flow CNN—revisiting data fidelity and regularization. *IEEE Trans. Pattern Anal. Mach. Intell.* **43**, 2555–2569 (2021).
- Sim, H. et al. XVFI: eXtreme video frame interpolation. In IEEE/CVF International Conference on Computer Vision (ICCV) 14469–14478 (IEEE, 2021).

- 39. Upchurch, P. et al. Deep feature interpolation for image content changes. In 2017 IEEE Conference on Computer Vision and Pattern Recognition (CVPR) 6090–6099 (IEEE, 2017).
- Liu, X. et al. Image interpolation via regularized local linear regression. *IEEE Trans. Image Process.* 20, 3455–3469 (2011).
- 41. Blu, T., Thévenaz, P. & Unser, M. Linear interpolation revitalized. *IEEE Trans. Image Process.* **13**, 710–719 (2004).
- 42. Brynolfsson, P. et al. Haralick texture features from apparent diffusion coefficient (ADC) MRI images depend on imaging and pre-processing parameters. *Sci. Rep.* **7**, 4041 (2017).
- 43. Haralick, R. M., Dinstein, I. & Shanmugam, K. Textural features for image classification. *IEEE Trans. Syst. Man Cybern.* **3**, 610–621 (1973).

Publisher's note Springer Nature remains neutral with regard to jurisdictional claims in published maps and institutional affiliations.

Open Access This article is licensed under a Creative Commons Attribution-NonCommercial-NoDerivatives 4.0 International License, which permits any non-commercial use, sharing, distribution and reproduction in any medium or format, as long as you give appropriate credit to the original author(s) and the source, provide a link to the Creative Commons licence, and indicate if you modified the licensed material. You do not have permission under this licence to share adapted material derived from this article or parts of it. The images or other third party material in this article are included in the article's Creative Commons licence, unless indicated otherwise in a credit line to the material. If material is not included in the article's Creative Commons licence and your intended use is not permitted by statutory regulation or exceeds the permitted use, you will need to obtain permission directly from the copyright holder. To view a copy of this licence, visit http://creativecommons.org/licenses/by-nc-nd/4.0/.

© The Author(s) 2025

Methods

Specimen acquisition

A sample of nondiseased human pancreas tissue was stained with H&E; another similar sample was stained with leukocyte marker CD45 via IHC (denoted IHC-CD45). Both samples were from individuals who underwent surgical resection for pancreatic cancer at the Johns Hopkins Hospital². The H&E dataset consisted of a stack of 101 serially sectioned slides at a resolution of $2\times2\times4~\mu m$. H and E are standard histological stains that mark nuclei and cellular structures (H) and ECM (E), respectively. The IHC-CD45 dataset consisted of 275 consecutive slides in which every third section (16 μm apart) was stained, at a resolution of $2\times2\times16~\mu m$, and is as described in Kiemen et al. 44 . CD45 is a general marker for leukocytes. This retrospective study was approved by the Johns Hopkins University Institutional Review Board.

A stack of ssTEM micrographs within a densely annotated mouse visual cortex petascale image volume (public dataset Minnie65) was obtained through the online Brain Observatory Storage Service and Database, created and managed by the Johns Hopkins Applied Physics Laboratory. This dataset consisted of 100 ssTEM slides captured at a resolution of $8\times8\times40$ nm² (ref. 7).

Light-sheet microscopy images of mouse lung were obtained from the Image Data Resource public repository 17,45 . This dataset consisted of 401 serial light-sheet microscopy images captured at a resolution of $3.22\times3.22\times10~\mu m$.

MRI samples of human brain were obtained from the Amsterdam Open MRI Collection (AOMIC) 46 . Specifically, the PIOP2 (Population Imaging of Psychology) cohort consisting of structural MRI scans of students was used. The dataset consisted of 220 structural MRI scans captured at a resolution of $1\times1\times1$ mm.

Segmentation of pancreatic microanatomy in histology slides

The previously developed semantic segmentation model CODA was leveraged to segment WSIs of H&E-stained pancreas samples into their different microanatomical components 2,10,47 . CODA was specifically trained for the segmentation of microanatomical components of the pancreas and labeled seven components at a resolution of 2 μm per pixel, including islets of Langerhans, ductal epithelium, blood vessels, fat, acini, ECM and pancreatic intraepithelial neoplasia (PanIN), which are precursor lesions of pancreatic cancer 2 .

Interpolation between 2D images

Spatial interpolation between 2D slides within a stack was carried out by developing InterpolAI, which is based on FILM, a model previously developed for temporal interpolation between frames of videos by Reda et al.³⁴. The model uses a three-step process to interpolate intermediate frames between two input images: a feature extraction pyramid, optical flow estimation and feature fusion and frame synthesis.

The feature extraction pyramid consists of six convolutional layers responsible for extracting features from the input images, each with increasing kernel size and decreasing stride capturing progressively larger receptive fields, extracting features from coarser to finer scales. This coupled with the use of shared weights across scales, allows the model to extract features for both small and large motions efficiently.

The features extracted are then fed into a bidirectional optical flow estimation module. This module calculates the pixel-wise motion vectors (or 'flows') between the features of two input images at each pyramid level. These flows represent the transformation needed to warp the features from one frame to the other. The bidirectional approach allows the model to capture both forward and backward motion, leading to more accurate and detailed interpolations³⁴.

With the extracted features and estimated flows, FILM enters the final fusion stage. The aligned features from both input images, along with the flows and the original input images themselves, are concatenated into a single feature pyramid. This captures both the feature information and the motion dynamics between the two frames. Finally,

a U-Net decoder architecture processes this fused feature pyramid and synthesizes the final interpolated frame. The U-Net's skip connections, which bypass several layers within the network and concatenate their outputs directly with the outputs of later layers, ensures that the interpolated frame retains fine details and maintains consistency with the input images³⁴.

FILM used a recursive function (equation (1)), which accounted for the number of input frames, n, and the number of recursive passes over which the model would interpolate, k. This limited the number of frames that could be interpolated between the input images to be either one, four, seven or fifteen frames (equation (1)).

$$f = 2^{k} (n-1) - 1 \tag{1}$$

Recognizing the need for flexibility in skipping slides based on user requirements, a time series spanning from 0 to 1 was implemented in InterpolAI, with step sizes dynamically determined by the number of skipped slides. This approach generated time points corresponding to the skipped slides, facilitating variable frame interpolation between input pairs.

InterpolAl was pretrained on the Vimeo-90k dataset, a largescale dataset of 89,800 high quality videos designed specifically to train models oriented toward video processing tasks such as frame interpolation, image denoising and resolution enhancement ³⁴. The optical flow of this model is already robustly pretrained on a diverse set of videos with different moving objects, such as vehicles, people and smaller features such as cameras and soccer balls. Retraining of the model posed two challenges: a lack of documentation on retraining and perfectly registering histological slides to curate a training dataset. The focus of InterpolAl on optical flow means that the model is sensitive to misalignment in the training images, making histological slides an unfavorable dataset to retrain the optical flow model due to inherent variability in tissue preparation, staining intensities and sectioning processes, which lead to unpredictable distortions and variations that complicate accurate spatial alignment of a stack of slides.

For large images such as those encountered in histology, InterpolAI provides a tile-and-stitch algorithm to efficiently handle computer memory limitations. WSIs are tiled to a user defined size of 1,024 or 2,048 padded tiles each with an \boldsymbol{x} and \boldsymbol{y} index. Tiled images with the same \boldsymbol{x} and \boldsymbol{y} index are then used as inputs to interpolate images. Once all tiles are interpolated for each tile pair, the tiles are stitched back together with the pad area removed for each respective interpolated \boldsymbol{z} slide. This ensures the robustness of InterpolAI for not only small but large images at high magnification.

Two versions of the InterpolAl code were developed, a validation code and an operation code. The validation code uses a skip-count algorithm such that the image being interpolated exists in the provided folder path but was simply skipped and generated similarly to how it is presented in this study. The validation code then computes the Haralick texture features of both the skipped authentic image and the respective interpolated image. All Haralick scores are saved into .csv file from which PCA analysis can be carried out. The operation code has a skip-count algorithm that generates images between each image pair in the provided folder path without skipping any image, thereby generating missing images.

Registration assessment

To understand and quantify the alignment needed for image interpolation, the H&E dataset was used. Four different types of misalignment were considered, including a vertical shift, horizontal shift, diagonal shift and rotation (Supplementary Fig. 1). Using aligned slides at z=31 and 33 from the H&E dataset, a 3,024 \times 3,024 tile was cropped from both WSIs at the same position. For shift misalignment, the 3,024 \times 3,024 tile from slide 31 was shifted horizontally, vertically and diagonally from 0 to 200 μm and then cropped to a 1,024 \times 1,024 tile from the center,

whereas slide 33 was left unshifted and cropped to a 1,024 \times 1,024 tile from the center of the 3,024 \times 3,024 tile. For rotation misalignment, the 3,024 \times 3,024 tile from slide 31 was rotated 0 to 200 degrees from its center and then cropped to a 1,024 \times 1,024 tile from the center, while slide 33 was left unrotated and cropped to a 1,024 \times 1,024 tile from the center of the 3,024 \times 3,024 tile. At a resolution of 2 \times 2 \times 4 μ m a 1-degree rotation from the center of a 3,024 \times 3,024 tile corresponds to a 75- μ m misalignment at the furthest edges from the center of a 1,024 \times 1,024 tile, as shown below:

Image_{center} =
$$\left(\frac{3,024}{2}, \frac{3,024}{2}\right)$$
 = (1,512, 1,512)

Considering the misalignment of the furthest point from the center, the distance from the center to the corner (R) is given by:

$$R = \sqrt{(1,512)^2 + (1,512)^2} = 2,138.6$$
 pixels

$$R_{\text{um}} = 2,138.6 \text{ pixels} * 2 \mu\text{m/pixel} = 4,277.2 \mu\text{m}$$

Using arc length formula (equation (2)) the maximum displacement (Δs) at the edge furthest from the center of the image can be calculated as:

$$\Delta s = R_{\text{um}} \times \theta \tag{2}$$

Calculating for a rotation of one degree:

$$\theta = \frac{1 \times \pi}{180} = 0.01745 \, \text{radians}$$

$$\Delta s = 4,277.2 \, \mu m \times 0.01745 = 74.6 \, \mu m$$

Interpolation using InterpolAI, linear interpolation and XVFI was conducted between shifted and rotated slide 31 and unchanged slide 33 to generate slide 32, which was then correlated to the authentic slide 32 using Pearson correlation. The Pearson correlation was calculated using the SciPy stats package available in Python.

Haralick texture features

Thirteen Haralick texture features were calculated to provide a quantitative representation of the texture patterns within an image, offering insights into their spatial arrangements and relationships 42,43 . The 13 features measure the angular second moment, contrast, correlation, sum of squares variance, inverse difference moment, sum average, sum variance, difference variance, sum entropy, difference entropy, entropy, information measure of correlation 1 and information measure of correlation 2 (refs. 42,43). Contrast measures the intensity variations between neighboring pixels, correlation gauges the linear dependency of gray levels, energy represents the image uniformity and homogeneity measures the closeness of gray level pairs.

To manage the complexity and high dimensionality of the feature space, dimensionality reduction was carried out using PCA. PCA transformed the original set of Haralick features into a reduced set of principal components, retaining the most important information while discarding redundant or less informative aspects. This reduction not only simplifies the interpretation of the data, but also allows for a holistic assessment of image quality, capturing the essential texture information in a more compact form.

Additionally, analysis of the Euclidean distances between authentic and interpolated images was computed using the 13 Haralick features. By considering the Euclidean distances across all selected Haralick features simultaneously, a comprehensive evaluation of the overall error value was achieved. This validation process ensured that

the collective impact of texture features was considered, providing a robust measure of similarity and/or dissimilarity between images. The combination of Haralick texture features, PCA for dimensionality reduction and Euclidean distance computation offered a systematic and effective approach for evaluating image quality and texture patterns.

Cell detection in histological sections

To validate the (synthetic) interpolated H&E and IHC images, the CODA cell detection module was used to count the total number of cells in H&E images and CD45 $^+$ cells in IHC and compare these numbers with those in their respective authentic images 2 . For this task, the intensity range of blue pixels was first determined for the nuclei of cells, along with the intensity of brown pixels for positive CD45 stain. Using k-means clustering, the mode blue pixel intensity was determined and selected to represent the hematoxylin channel, while the mode brown pixel intensity was selected to represent the positive stain. With color deconvolution, the cells stained with hematoxylin could be extracted from the remaining tissue, thereby providing a cell count.

Quantification of damage

To understand and quantify the quality of input images required for image interpolation, a damage assessment was carried out on a subset of the last 25 consecutive slides from the H&E dataset and 25 images of the ssTEM dataset (Supplementary Fig. 2). A CODA segmentation model was trained to detect folds in both datasets and segment them as damage. Next, interpolation of both datasets was carried out while skipping three authentic images and interpolating them. The interpolated images were subsequently segmented using the same CODA segmentation model to detect folds as was done with the authentic images. Using the segmented images, the difference in the total number of folded pixels between the interpolated images and authentic images was determined and divided by the total number of folded pixels in the authentic images to determine the percentage by which damaged was reduced through interpolation (Supplementary Fig. 2b,f). Segmented images were also used to plot the folds in both datasets in 3D and show the reduction in folds through interpolation. The number of folded pixels in individual 2D images was plotted against the size of the fold in 3D to obtain a log-log plot of the reduction in folds in 3D, as a result of interpolation (Supplementary Fig. 2c,g).

3D rendering of interpolated 2D images

InterpolAI was used to interpolate stacks of WSIs of missing or damaged slides, which resulted in a whole restored dataset (Fig. 1b). For image postprocessing, CODA was used to semantically segment histological slides and MRI images to reconstruct microanatomical tissue structures and whole organs in 3D (Fig. 1b)². Through manual annotations of microanatomical tissue structures in a small subset of histology slides and whole organ annotations of the brain in a subset of MRI images, CODA allowed for two deep learning models to be trained to recognize these annotations and apply them to the remaining slides and/or images in the respective datasets, thereby generating stacks of segmented histology slides and MRI images. Labels within the segmented slides and/or images, corresponding to the annotations could then be used by CODA to reconstruct and visualize 3D tissue structures of interest, such as epithelial ducts in the pancreas and whole organs such as the brain. Similarly, CODA was leveraged to 3D reconstruct synapses in the mouse brain using presegmented ssTEM slides with the appropriate synapse label. Tissue-cleared light-sheet images were separated into their respective red, green and blue channels allowing for three stacks to be obtained, one for each channel. 3D reconstructions of structures within the tissue-cleared light-sheet images of the lung were then generated by creating volumes using stacks of channel-separated images. Specifically, the red channel was used to reconstruct the bronchioles in the mouse lung.

Computing hardware and software

We used Python (v.3.9) and Tensorflow (v.2.10.0) for all image interpolations and analysis. For the CODA quantifications and 3D renderings, we used MATLAB (2023a).

For smaller sized images, computers equipped with a single NVIDIA RTX 3090 graphical processing unit (GPU) could easily interpolate them. For larger WSIs, with dimensions exceeding 14,000 × 10,000 pixels, using more GPU power allowed to speed up the interpolation processing times. To handle these larger images with higher magnifications, we used the Rockfish cluster at Johns Hopkins University, which is equipped with nodes containing four NVIDIA A100 GPUs each. This high-performance computing resource enabled us to interpolate whole slide histological images in shorter times. In case of no access to GPU clusters, users may opt for a tile-and stitch approach provided in our code, which allows for tiling of large WSIs, interpolating the tiles individually and then stitching them back together into WSIs during postprocessing. The codes and requirements for InterpolAI have been posted on GitHub.

Reporting summary

Further information on research design is available in the Nature Portfolio Reporting Summary linked to this article.

Data availability

Data are available upon request from the corresponding author. The light-sheet lung dataset analyzed in this paper is available at https://doi.org/10.1038/s42003-021-01786-y (ref. 17). The ssTEM dataset analyzed in this paper is available at https://doi.org/10.60533/BOSS-2021-TOSY (ref. 48). The MRI dataset analyzed in this paper is available at https://doi.org/10.18112/openneuro.ds002790.v2.0.0 (ref. 49).

Code availability

Software used in this paper can be accessed at https://github.com/sjoshi17jhu/InterpolAl.

References

- 44. Kiemen, A. L. et al. 3D histology reveals that immune response to pancreatic precancers is heterogeneous and depends on global pancreas structure. Preprint at bioRxiv https://doi.org/10.1101/ 2024.08.03.606493 (2024).
- Williams, E. et al. Image Data Resource: a bioimage data integration and publication platform. Nat. Methods 14, 775–781 (2017).
- Snoek, L. et al. The Amsterdam Open MRI Collection, a set of multimodal MRI datasets for individual difference analyses. Sci. Data 8, 85 (2021).
- 47. Braxton, A. M. et al. 3D genomic mapping reveals multifocality of human pancreatic precancers. *Nature* **629**, 679–687 (2024).
- IARPA MICrONS Minnie. BossDB https://doi.org/10.60533/BOSS-2021-TOSY (2025).

 Snoek, L. et al. AOMIC-PIOP2. OpenNEURO https://openneuro. org/datasets/ds002790/versions/2,0.0 (2020).

Acknowledgements

We acknowledge the following sources of support: grant nos. U54CA268083; UG3CA275681; R24MH114785 and U54AR081774; a Lustgarten Foundation-AACR Career development award for pancreatic cancer research in honor of Ruth Bader Ginsburg; Susan Wojcicki and Denis Troper; The Carl and Carol Nale Fund for Pancreatic Cancer Research; Rolfe Pancreatic Cancer Foundation; Ministerio de Ciencia, Innovación y Universidades (grant no. PID2019-109820RB-I00) and the European Regional Development Fund (ERDF); Universidad Carlos III de Madrid. HOPTEC student exchange program (Instituto Superior Técnico and Johns Hopkins University) and Fundação Luso-Americana para o Desenvolvimento (FLAD).

Author contributions

D.W., S.J., A.F., A.L.K. and P.-H.W. conceived the project. D.W., A.L.K., P.-H.W. and A.M.B. supervised the study. A.L.K. and A.F. collected and processed the human pancreas samples. D.X., J.M. and B.W. collected the mouse brain samples. S.J. and A.F. collected and processed the mouse lung and human brain samples. S.J., A.F., K.S.H., Y.S. and P.-H.W. conducted the image analysis, quantifications and validation. S.J., A.F., A.L.K. and D.W. wrote the first draft of the manuscript, which all authors edited and approved.

Competing interests

The authors declare no competing interests.

Additional information

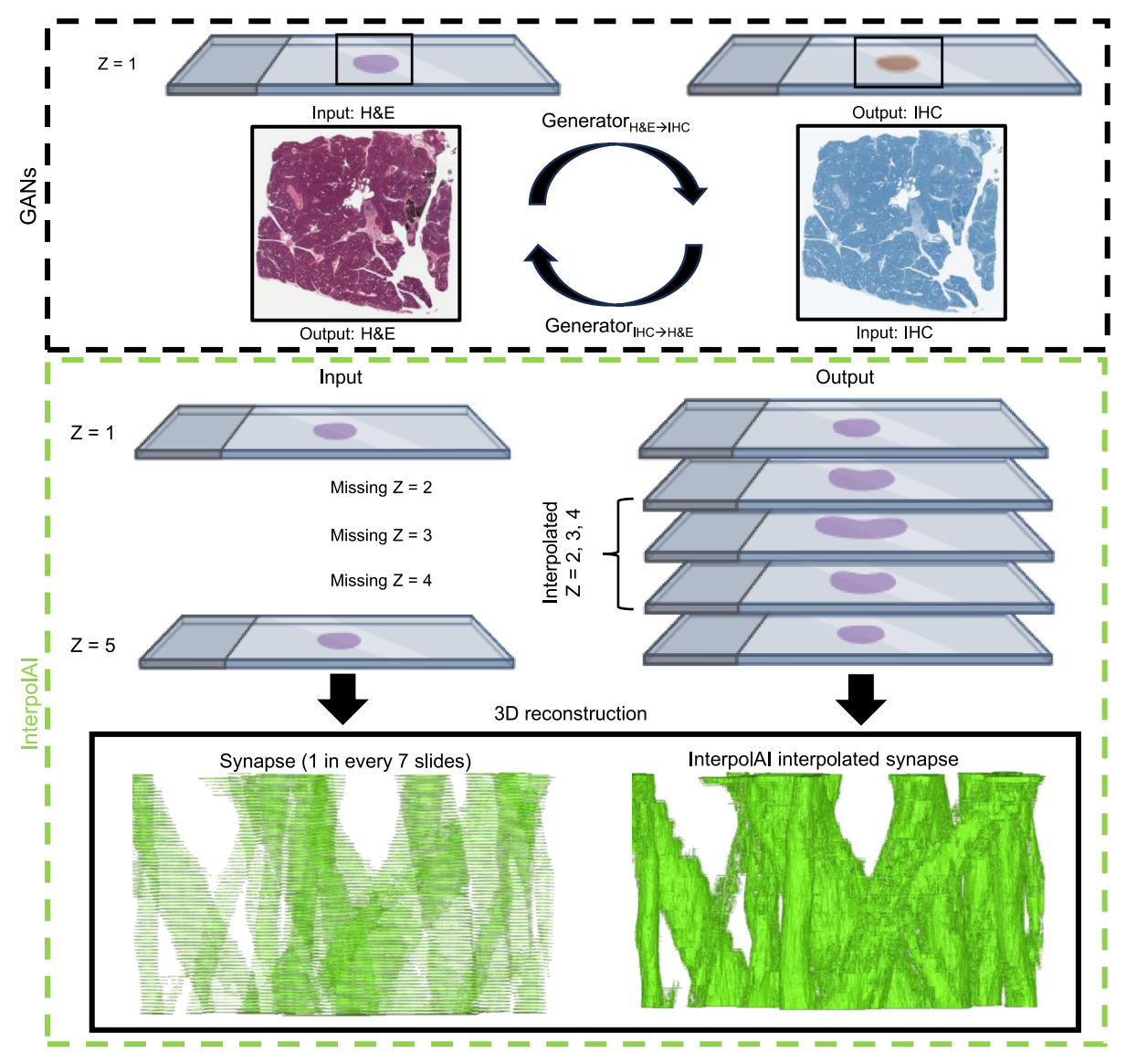
Extended data is available for this paper at https://doi.org/10.1038/s41592-025-02712-4.

Supplementary information The online version contains supplementary material available at https://doi.org/10.1038/s41592-025-02712-4.

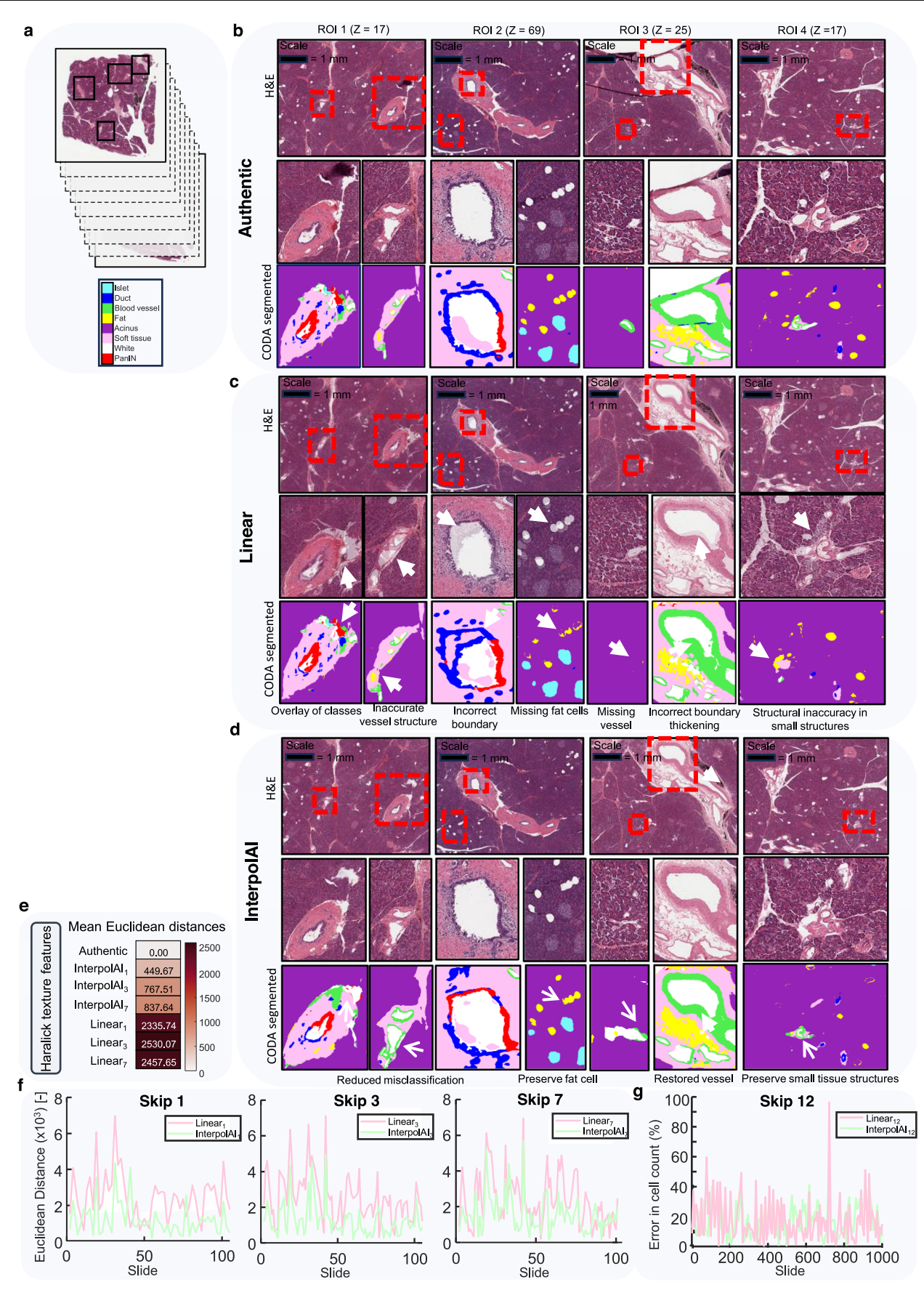
Correspondence and requests for materials should be addressed to Denis Wirtz.

Peer review information *Nature Methods* thanks Kianoush Falahkheirkhah and the other, anonymous, reviewer(s) for their contribution to the peer review of this work. Primary Handling Editor: Rita Strack, in collaboration with the *Nature Methods* team.

Reprints and permissions information is available at www.nature.com/reprints.



Extended Data Fig. 1 | A Fundamental comparison between GANs and Interpolal interpolation. GANs translate an H&E stained slide to a slide stained with IHC and vice versa (top panel). Interpolal interpolates multiple novel slides between two input slides, restoring tissue connectivity (bottom panel). Illustrations created using BioRender.com.



 $\textbf{Extended Data Fig. 2} \, | \, \textbf{See next page for caption.} \\$

Extended Data Fig. 2 | Qualitative comparison of linear and InterpolAl interpolations to authentic H&E-stained histological slides of a human pancreas when skipping 7 slides for four different ROI's. (a) Four ROIs were selected from H&E-stained whole slide images (WSI's). Slides were interpolated when skipping 7 slides between adjacent sections, thereby generating 7 slides. (b) The top row of authentic images shows the middle skipped z-slide of all four different ROIs selected for interpolation. The middle row of zoom-ins of authentic images shows microanatomical structures observed within the different ROI's. The third row of zoom-ins shows the CODA classification of these microanatomical structures. (c) The top row of linearly interpolated images shows the middle interpolated z-slide of all four different ROI's corresponding to the authentic images. The middle row of zoom-ins of linearly interpolated images

shows microanatomical structures generated by linear interpolation within the different ROI's. The third row of zoom-ins shows the CODA classification of these linearly interpolated microanatomical structures. (d) The top row of InterpolAI interpolated images shows the middle interpolated z-slide of all four different ROI's corresponding to the authentic images. The middle row of zoom-ins of InterpolAI interpolated images shows microanatomical structures generated by InterpolAI within the different ROI's. The third row of zoom-ins shows the CODA classification of these InterpolAI interpolated microanatomical structures. (e) Euclidean distance by slide of interpolated images from authentic images based on thirteen Haralick features for ROI1 and ROI2. (f) Percent error in CD45+ cell count by slide between authentic and interpolated images when skipping 12 slides.

nature portfolio

Corresponding author(s):	Dr. Denis Wirtz
Last updated by author(s):	Apr 9, 2025

Reporting Summary

Nature Portfolio wishes to improve the reproducibility of the work that we publish. This form provides structure for consistency and transparency in reporting. For further information on Nature Portfolio policies, see our <u>Editorial Policies</u> and the <u>Editorial Policy Checklist</u>.

~ .			
St	at	ıstı	$1 \cap S$

For	all st	atistical analyses, confirm that the following items are present in the figure legend, table legend, main text, or Methods section.
n/a	Cor	nfirmed
		The exact sample size (n) for each experimental group/condition, given as a discrete number and unit of measurement
	\boxtimes	A statement on whether measurements were taken from distinct samples or whether the same sample was measured repeatedly
	\boxtimes	The statistical test(s) used AND whether they are one- or two-sided Only common tests should be described solely by name; describe more complex techniques in the Methods section.
X		A description of all covariates tested
		A description of any assumptions or corrections, such as tests of normality and adjustment for multiple comparisons
	\boxtimes	A full description of the statistical parameters including central tendency (e.g. means) or other basic estimates (e.g. regression coefficient) AND variation (e.g. standard deviation) or associated estimates of uncertainty (e.g. confidence intervals)
	\boxtimes	For null hypothesis testing, the test statistic (e.g. <i>F</i> , <i>t</i> , <i>r</i>) with confidence intervals, effect sizes, degrees of freedom and <i>P</i> value noted Give <i>P</i> values as exact values whenever suitable.
\times		For Bayesian analysis, information on the choice of priors and Markov chain Monte Carlo settings
\boxtimes		For hierarchical and complex designs, identification of the appropriate level for tests and full reporting of outcomes
		Estimates of effect sizes (e.g. Cohen's d , Pearson's r), indicating how they were calculated
		Our web collection on <u>statistics for biologists</u> contains articles on many of the points above.

Software and code

Policy information about availability of computer code

Data collection

The software used in this manuscript is publicly accessible at : https://github.com/sjoshi17jhu/InterpolAI. The following packages were used in the operation of our code: python=3.9, cudatoolkit=11.2, cudnn=8.1.0, tensorflow<2.11, numpy==1.21.6, imageio, natsort, tqdm, jupyter

Data analysis

The software used for data analysis is as follows: mahotas=1.4.13 (for haralick features), CODA (cell detection), and Matlab R2023a.

For manuscripts utilizing custom algorithms or software that are central to the research but not yet described in published literature, software must be made available to editors and reviewers. We strongly encourage code deposition in a community repository (e.g. GitHub). See the Nature Portfolio guidelines for submitting code & software for further information.

Data

Policy information about availability of data

All manuscripts must include a data availability statement. This statement should provide the following information, where applicable:

- Accession codes, unique identifiers, or web links for publicly available datasets
- A description of any restrictions on data availability
- For clinical datasets or third party data, please ensure that the statement adheres to our policy

Data is available upon request from the corresponding author. The light-sheet lung dataset analyzed in this manuscript is available at the following DOI: 10.1038/

,		raset analyzed in this manuscript is available at the following DOI: 10.60533/BOSS-2021-TOSY. The MRI dataset analyzed in this ing DOI:10.18112/openneuro.ds002790.v2.0.0.			
Human rese	arch part	icipants			
Policy information	about <u>studies</u>	involving human research participants and Sex and Gender in Research.			
Reporting on sex	and gender	Not applicable.			
Population characteristics		Not applicable.			
Recruitment		Not applicable			
Ethics oversight		Not applicable			
ote that full informa	ation on the app	roval of the study protocol must also be provided in the manuscript.			
ield-spe	ecific re	eporting			
<u> </u>		is the best fit for your research. If you are not sure, read the appropriate sections before making your selection.			
Life sciences		Behavioural & social sciences			
		n all sections, see nature.com/documents/nr-reporting-summary-flat.pdf			
ifa sciar	ncas st	udy design			
l studies must dis		e points even when the disclosure is negative.			
Sample size	microscopy, n pancreas, hun range of biom was available	study was carried out using two cohorts: human and mouse. Four imaging modalities were studied: histology, tissue-clearing/light-sheet ascopy, magnetic resonance imaging, serial section transmission electron microscopy. Four different tissue types were used: human reas, human brain, mouse brain, and mouse lung. This diverse set of data was selected to demonstrate the applicability of our model to a e of biomedical images with varying resolutions. For all histology, tissue-clearing/light-sheet microscopy and MRI the whole sample which available was used, all slides/images. For ssTEM 100 slides were selected from the middle of the volume due to computational limitations a downloading the entire volume which is greater than 1 petabyte in size.			
Data exclusions	No data was e	xcluded.			
Replication	Defined and set weights used for image generation in this study have been provided in the github repository. Since weights dot not change after being defined, image generation for the same results is obtainable using the same datasets provided.				
Randomization	Samples were	Samples were divided by the imaging modality used to obtain them. Ie. Histology (H&E and IHC), Radiology (MRI), etc			
Blinding	Not relevant to this study, all metrics were computed for analysis.				
Reportin	g for s	pecific materials, systems and methods			
/e require informati	on from author	s about some types of materials, experimental systems and methods used in many studies. Here, indicate whether each materials your study. If you are not sure if a list item applies to your research, read the appropriate section before selecting a response.			
Materials & exp	perimental	systems Methods			
n/a Involved in the study		n/a Involved in the study			
N A satisfaction					

Materials & experimental systems		Methods	
n/a	Involved in the study	n/a	Involved in the study
\boxtimes	Antibodies	\boxtimes	ChIP-seq
\boxtimes	Eukaryotic cell lines	\boxtimes	Flow cytometry
\boxtimes	Palaeontology and archaeology	\boxtimes	MRI-based neuroimaging
\times	Animals and other organisms		
\boxtimes	Clinical data		
\boxtimes	Dual use research of concern		